A Generalized Sparse Bayesian Learning Algorithm for Near-Field Synthetic Aperture Radar Imaging: By Exploiting Impropriety and Noncircularity

Pan Long, Bi Dongjie, Li Xifeng, Xie Yongle

Abstract—The near-field synthetic aperture radar (SAR) imaging is an advanced nondestructive testing and evaluation (NDT&E) technique. This paper investigates the complex-valued signal processing related to the near-field SAR imaging system, where the measurement data turns out to be noncircular and improper, meaning that the complex-valued data is correlated to its complex conjugate. Furthermore, we discover that the degree of impropriety of the measurement data and that of the target image can be highly correlated in near-field SAR imaging. Based on these observations, A modified generalized sparse Bayesian learning algorithm is proposed, taking impropriety and noncircularity into account. Numerical results show that the proposed algorithm provides performance gain, with the help of noncircular assumption on the signals.

Keywords—Complex-valued signal processing, synthetic aperture radar (SAR), 2-D radar imaging, compressive sensing, Sparse Bayesian learning.

I. INTRODUCTION

NEAR-FIELD synthetic aperture radar (SAR) imaging techniques are derived from millimeter-wave and microwave holography that utilizes complex-valued data measured over a two-dimensional aperture to reconstruct a focused image of the target [22]. Near-field SAR imaging is well suited for the nondestructive testing and evaluation (NDT&E) since the operating millimeter-wave and microwave are non-ionizing, readily penetrate non-metal surface material (e.g. composites) and interact with the inner structure to render high-quality imagery [15].

However, for a typical near-field monostatic SAR system, in order to achieve high spatial resolution, it is demanded to scanning the target scene at high sampling rates in both frequency and space domains to satisfy the Shannon-Nyquist sampling criterion [5], [25]. Therefore, the data acquisition process will be time-consuming. For instance, the conventional uniform sampling requires about one hour to scan a 120 $\times$ 180 mm^2 area at 2-mm step size. Significant amount of time is wasted in moving and pinpointing the antenna probe. By contrast, the scanning procedure is quite fast, hence it is usual practice that near-field monostatic SAR imaging system operates multi-frequencies scanning rather than single-frequency scanning.

The compressive sensing (CS) methodology, received much attentions in recent years [6], [20], have shown great potential in reducing the measurement time via randomly sensing a very limit fractional number of spatial points in the entire scanning plane. In this paper, we consider the near-field SAR imaging problem in the CS framework. As one of the state-of-the-art CS algorithms, the approximate message passing (AMP) algorithm and its variants have shown to be effective and efficient [13], [17], [19]. In general, advantages of the AMP algorithms include: 1) encode prior distribution flexibly; 2) provide the uncertain degrees of the estimates [2]; 3) avoid matrix inversion [9].

The measurement data in near-field SAR system contains phase and amplitude information, is expressed as complex-valued. To consider CS algorithms for such complex-valued signals, literature fall into two categories: 1) by decoupling real and imaginary parts or by simply using amplitude constraints [10]; 2) by applying smoothness constraint on phase as well as amplitude [26].

The latter category suggests a smoothing constraint on the phase information, aims mainly to enhance robustness and deal with discontinuities in data acquisition [8]. The work in [8], [24], [26], [11] have shown comprehensive performance improvement by using the smoothing prior information.

For the former category, there are two major disadvantages. First, the rearranged real-valued data is twice the scale of the original complex-valued data in the processing, and similarly, the sensing matrix becomes four times of the original one [7], which increase the computational complexity significantly. Second, as reported in [23], [16], in many application the real and imaginary parts tend to be either zero or non-zero simultaneously, so decomposition without considering such extra information may lead to performance degradation. Modifications has been made in [23], where the real and imaginary components are treated jointly.

In this paper, we further extend the work in [23] by considering correlation between the real and imaginary parts, in terms of covariance and pseudo-covariance (also called complementary covariance). The idea comes from statistical processing of complex-valued random variables [21], which has two key ingredients: 1) full statistical characterization [1] of complex-valued data; 2) optimization over complex parameters [2] [16].

Based on the observation that the near-field SAR signal has (high level) non-circular or improper nature (details are

---

[1]Impropriety and non-circularity of the complex-valued data (or random processes) are taken into account, the definition of which are given in Section III.

[2]For necessary tools including widely linear transformations, augmented statistical descriptions, and Wirtinger calculus, we refer the reader to [21]

Pan Long is with University of Electronic Science and Technology of China, Chengdu (e-mail: panlong2016@gmail.com).

World Academy of Science, Engineering and Technology
International Journal of Electronics and Communication Engineering
Vol:13, No:5, 2019

given in Section III), especially in near range scanning setting, the proposed algorithm considering impropriety (second-order non-circularity) provides performance gain. Note that statistics (such as non-circular and second-order non-circular) are correspond to (stationary) random processes, and the multi frequencies collection in our application can provide sufficient data (as samples of a random variable) for calculating a relatively stationary statistics (details are given in Section III).

The organization of the paper is as follows. In Section II, we present brief review of the near-field SAR holographic image reconstruction. In Section III, We take a close look at second-order non-circular of the near-field SAR measurement data. In Section IV, the proposed complex-valued generalized sparse Bayesian learning algorithm is presented. In Section V, numerical experiment to compare the performance of different CS algorithms is conducted. And Section VI concludes the paper.

II. NEAR-FIELD SAR IMAGING

A. Two-Dimensional Near-Field SAR Image Reconstruction

The measurement configuration of the near-field SAR imaging system is shown in Fig. 1. The coordinate of antenna is identified by $s(x', y', z_0)$. Data acquisition is performed by moving the antenna probe in uniform step on the scanning (aperture) plane. The target is placed at the distance z_0 from the scanning plane, of which a general point is identified as (x, y, z). The target is assumed to be flat, parallel to the (x, y, z_0)-plane, and fully characterized by the reflective function $f(x, y, z)$, which is defined as the ratio of reflected field to incident field [22]. Our goal is to reconstruct the reflective function (i.e. the target image) from the reflected measurement data.
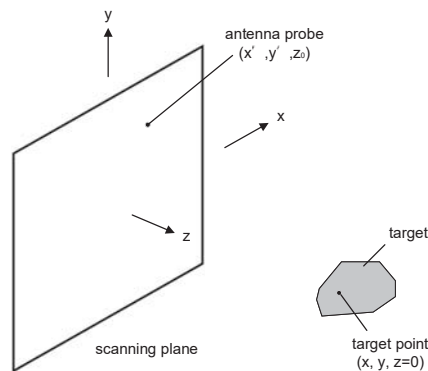

Fig. 1 Data (or reflected wave) acquisition model of near-field SAR imaging system

We begin with the response at antenna probe, which is the superposition of reflection from each point on the target multiplied by the round-trip phase to that point [22]:

$$s\left(x', y'\right) = \iint \underbrace{f(x, y, z)}_{\text{target}} \underbrace{e^{-j2k\sqrt{(x-x')^2+(y-y')^2+z_0^2}}}_{\text{spherical wave emanating from } (x', y')} dx dy$$
(1)

where $k = \frac{\omega}{c}$ denotes the wavenumber, ω and c denote temporal angular frequency and the speed of light,

respectively. The amplitude decay with range is neglectable in the near-field scenario.

The spherical wave can be decomposed into a superposition of plane-wave components

$$e^{-j2k\sqrt{(x-x')^2+(y-y')^2+z^2}}$$
$$= \iint e^{jk'_x(x'-x)+jk'_y(y'-y)+jk_z z_0} dk_{x'} dk_{y'}$$
(2)

where $k_{x'}$ and $k_{y'}$ are variables in Fourier domain corresponding to x' and y' respectively.

By using the definition of 2-D Fourier transform, the expression in (1) can be reorganized as [22]

$$s\left(x', y'\right) = \iint \underbrace{\left[\iiint f(x, y, z_0) e^{-j\left(k_{x'}x + k_{y'}y\right)} dx dy\right]}_{2D \text{ Fourier Transform of } f(x, y, z_0)}$$
$$\times e^{j\left(k_{x'}x' + k_{y'}y' + k_z z_0\right)} dk_{x'} dk_{y'}$$
(3)

The distinction between the primed and unprimed coordinate systems is dropped since the coordinate systems coincide [22]. Then the inversion for image then gives

$$f(x, y) = \mathcal{F}_{2D}^{-1}\left[\mathcal{F}_{2D}[s(x, y)] e^{-jk_z z_0}\right].$$
(4)

Follow dispersion relation for electromagnetic plane waves

$$k_x^2 + k_y^2 + k_z^2 = (2k)^2$$
(5)

$$k_z = \sqrt{4k^2 - k_x^2 - k_y^2}.$$
(6)

Finally, the reconstruction reads

$$f(x, y) = \mathcal{F}_{2D}^{-1}\left[\mathcal{F}_{2D}\{s(x, y)\} e^{-jz_0\sqrt{4k^2-k_x^2-k_y^2}}\right]$$
(7)

and is referred to as forward 2-D SAR transform [5], which converts the reflected data to the image, and the reverse procedure

$$s(x, y) = \mathcal{F}_{2D}^{-1}\left[\mathcal{F}_{2D}\{f(x, y)\} e^{jz_0\sqrt{4k^2-k_x^2-k_y^2}}\right]$$
(8)

is called reverse 2-D SAR transform [4].

B. Compressed Sensing SAR Image Reconstruction

In order to introduce the underdetermined linear measurement model for the near-field SAR imaging in a concise manner, we first reformulate the forward 2-D SAR transform in (7) as

$$\boldsymbol{\Phi}_2 = \boldsymbol{\Phi}_{2DFT}^H \times \left(\mathbf{E} \circ \boldsymbol{\Phi}_{2DFT}\right),$$
(9)

where $\circ$ denotes Hadamard product and $(\cdot)^H$ denotes transposition. $\boldsymbol{\Phi}_{2DFT}^H$ and $\boldsymbol{\Phi}_{2DFT}$ denote the 2-D Fourier transform and the inverse 2-D Fourier transform in matrix format, respectively. And the reverse 2-D SAR transform in (8) can be expressed as $\boldsymbol{\Phi}_2^H$, based on the fact that $\boldsymbol{\Phi}_{2DFT}$ is orthogonal.

World Academy of Science, Engineering and Technology
International Journal of Electronics and Communication Engineering
Vol:13, No:5, 2019

Then, we use matrix $\boldsymbol{\Phi}_1$ is to indicate the random sampling positions of the antenna probe is constructed with randomly distribution of the zero/one entries.

Next, we use $\boldsymbol{\Phi}_2$ to denote the transform that projects underlying target image to a wavelets domain. An orthogonal (or bi-orthogonal) wavelets will be a convenient choice to facilitate the inverse process. In this paper, the Symlet wavelets transform with eight vanishing moments is chosen as preset.

To summarize, with the overall sensing matrix composed of $\boldsymbol{\Phi} = \boldsymbol{\Phi}_1 \circ \boldsymbol{\Phi}_2^H \boldsymbol{\Phi}_3^H$, the sparse recovery problem is represented as

$$\mathbf{y} = \boldsymbol{\Phi}\mathbf{x} + \mathbf{n}, \tag{10}$$

where $\mathbf{y}$, $\mathbf{x}$ and $\mathbf{n}$ denote the measurement data, the underlying wavelets coefficients of the target image, and the Gaussian measurement noise, respectively.

III. COMPLEX-VALUED STATISTICS

In this section, we investigate a real-world experiment where improper (second-order non-circular) measuremnt data arises, and present two observations:

1) The complex-valued reflected data are improper (or second-order non-circular);
2) The degree of non-circularity of the reflected data is approximately equal to that of the target image.

A. The Improper Measurement Data

Fig. 2 (a) Photo of the sample before paint. (b) Photo of the specimen after paint

The experiment was conducted on a corrosion-under-paint sample operating at microwave frequencies uniformly spaced in 18 to 26.4 GHz (K-band), with step size 0.084 GHz (N_ω = 101). As shown in Fig. 2, the area of steel sheet under corrosion was about 32mm×32mm with thickness of 0.08mm, then the common paint with thickness of 0.6mm was sprayed over the steel sheet as uniformly as possible. The sample was placed below the antenna probe at a depth of $z_t = -1$mm, and an area of 64mm $\times$ 64mm was scanned with a uniform measurement grid of 2mm in both x- and y-directions and the fully sampled raw data had a dimension of 32×32.

We visualize the measurement data operated at frequency 19.596 GHz in Fig. 3. It is obvious that there is a strong negative correlation between the real and the imaginary part of the raw data. And measurement data collected with respect to other frequencies share the similar pattern.

In order to measure the degree of the correlation, we introduce the concept of pseudo covariance, which appears frequently in complex-valued random signal processing [21].

To calculate the pseudo covariance, we collect the complex-valued scalar located at (x, y, z) from each frequency layer, shown in Fig. 4 (a). These scalars $\{a_1 + ib_1, a_2 + ib_2, ..., a_{101} + ib_{101}\}^T$ can be seen as samples of a complex-valued random variable $\mathbf{x}_{\text{data}}$.

These samples are reflected data received at the same location, which are expected to share similar (or same) physical interpretations; hence random variable $\mathbf{x}_{\text{data}}$ can be assumed to have stationary statistics. In that sense, the covariance function $c(k, m)$ of $\mathbf{x}_{\text{data}}$ is defined as [1]

$$c(k, m) = E\{\mathbf{x}_{\text{data}}(k+m)\mathbf{x}_{\text{data}}^*(k)\} - \\ E\{\mathbf{x}_{\text{data}}(k+m)\}E\{\mathbf{x}_{\text{data}}^*(k)\} \tag{11}$$

where $E\{\mathbf{x}_{\text{data}}(k+m)\mathbf{x}_{\text{data}}^*(k)\}$ is the correlation function, and $\mathbf{x}_{\text{data}}^*(k)$ is the conjugate transposition of $\mathbf{x}_{\text{data}}(k)$. To fully characterize the second-order statistics, we follow the definition of pseudo covariance function in [1], given by

$$\tilde{c}(k, m) = E\{\mathbf{x}_{\text{data}}(k+m)\mathbf{x}_{\text{data}}(k)\} - \\ E\{\mathbf{x}_{\text{data}}(k+m)\}E\{\mathbf{x}_{\text{data}}(k)\}. \tag{12}$$

As shown in Fig. 4 (b), the pseudo covariance function does not vanishes for all pairs (k, m), therefore, random variable $\mathbf{x}_{\text{data}}$ is identified to be improper or second-order non-circular [1]. Note that the measurements at other location have similar statistics.

B. The Pseudo Covariances Are Highly Correlated

In this subsection, we additionally bring the target images into discussion, which are reconstructed from full-sampled reflected data via the forward 2-D SAR transform in Section II.

We assign a random variable $\mathbf{x}_{\text{data}}$ to represent a general point in the measurement data, with sample set $\{a_1 + ib_1, a_2 + ib_2, ..., a_{101} + ib_{101}\}$, in the same way as the above subsection; And likewise, we assign a random variable $\mathbf{x}_{\text{image}}$ to that of the target images, with sample set $\{c_1 + id_1, c_2 + id_2, ..., c_{101} + id_{101}\}$.

As shown in Figs. 5 (a) and (b), We pick a scalar at a typical location (e.i. index NO.692), of both target image and reflected data, as an illustration for calculating the pseudo covariance.

Follow the definition in [1], the augmented covariance matrix of a random vector or variable $\mathbf{x}$ is

$$\underline{\mathbf{C}}_{\mathbf{xx}} = E\left\{\underline{\mathbf{xx}}^H\right\} = \begin{bmatrix} \mathbf{C}_{\mathbf{xx}} & \tilde{\mathbf{C}}_{\mathbf{xx}} \\ \tilde{\mathbf{C}}_{\mathbf{xx}}^* & \mathbf{C}_{\mathbf{xx}}^* \end{bmatrix}. \tag{13}$$

The north-west block of matrix $\underline{\mathbf{C}}_{\mathbf{xx}}$ is the covariance matrix is the usual (Hermitian) covariance matrix

$$\mathbf{C}_{xx} = E\left\{\mathbf{x}\mathbf{x}^H\right\} = \mathbf{C}_{x_r x_r} + \mathbf{C}_{x_i x_i} + j\left(\mathbf{C}_{x_r x_i}^T - \mathbf{C}_{x_r x_i}\right) \tag{14}$$

with $\mathbf{C}_{x_r x_r} = E\left\{\mathbf{x}_r \mathbf{x}_r^T\right\}$, $\mathbf{C}_{x_r x_i} = E\left\{\mathbf{x}_r \mathbf{x}_i^T\right\}$, and $\mathbf{C}_{x_i x_i} = E\left\{\mathbf{x}_i \mathbf{x}_i^T\right\}$. The north-east block is the pseudo covariance matrix

World Academy of Science, Engineering and Technology
International Journal of Electronics and Communication Engineering
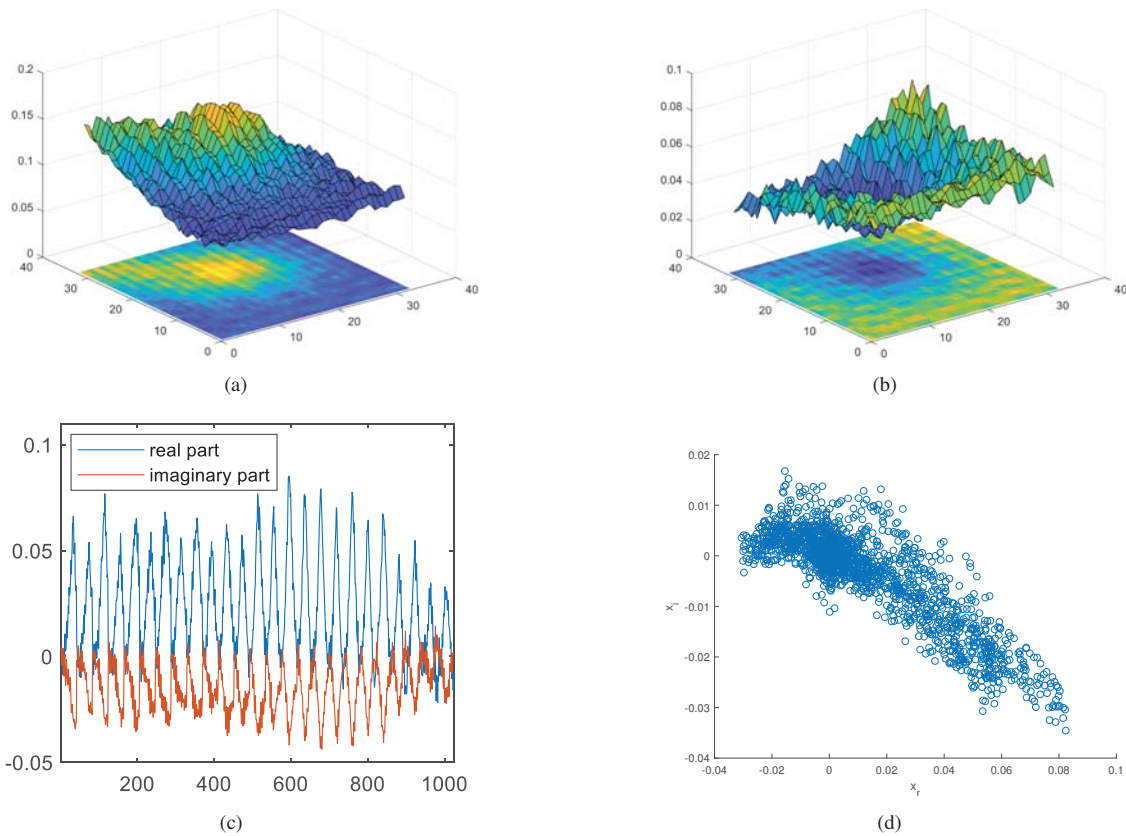Vol:13, No:5, 2019

(a)

(b)

(c)

(d)

Fig. 3 Reflected data of a single-frequency measurement (19.26 GHz) is collected in a 2-D matrix, dimension of which is 32×32. (a) The real parts. (b) The imaginary parts. (c) The reflected data is reshaped as a 1024×1 vector, the real and imaginary parts of which are plotted side-by-side. (d) Scatter plot of the 1024 complex-valued data, with "x_r" being the real axis and "x_i" being the imaginary axis

(a)

(b)
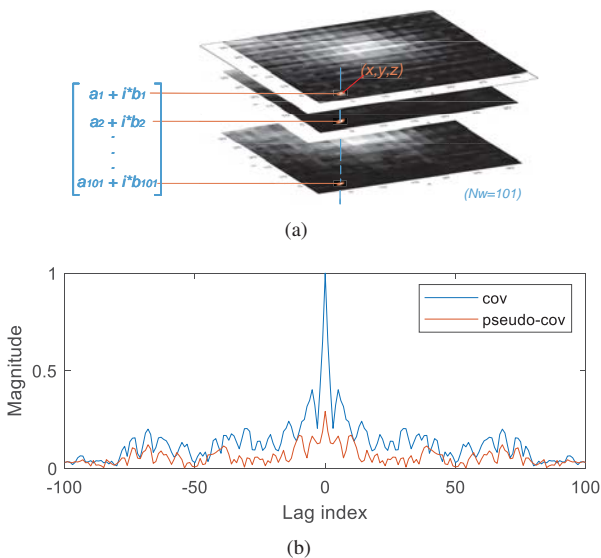
Fig. 4 (a) The multi-frequencies reflected data set is consist of data collected with $N_\omega = 101$ different scanning frequency, ranging from 18 GHz to 26.4 GHz; And the complex scalar at location (x,y,z) is extracted from each frequency layer, to build a sample set for the particular location. (b) The covariance function and the pseudo covariance function is calculated based on the sample set $\{a_1 + ib_1, a_2 + ib_2, ..., a_{101} + ib_{101}\}$

$$\tilde{\mathbf{C}}_{xx} = E\left\{\mathbf{x}\mathbf{x}^T\right\} = \mathbf{C}_{x_r x_r} - \mathbf{C}_{x_i x_i} + j\left(\mathbf{C}_{x_r x_i}^T + \mathbf{C}_{x_r x_i}\right)$$

$$(15)$$

which uses a regular transpose rather than a Hermitian (conjugate) transpose. Note that in the case of random variable, the covariance matrix and the pseudo covariance matrix will degenerate into scalars.

We calculate the pseudo covariance for all the random variables, and plot the results in Fig. 5 (b). The degree of non-circularity characterized by pseudo covariance of the reflected data is approximately equal to that of the target image.

IV. ALGORITHM FOR COMPLEX-VALUED PROCESSING

The observation in Section III allows us to reveal a deeper connection between measurements and underlying signal, and leads to a algorithmic modification of the unified sparse Bayesian learning [18], specialized to deal with impropriety.

First, we briefly review the unified generalized Bayesian framework (also called GrSBL) in [18].

Second, we replace the MMSE module in the generic framework with a component-wise widely linear MMSE, due to the fact that MMSE module in [18] can only be applied to the setting where posterior means and variances can be
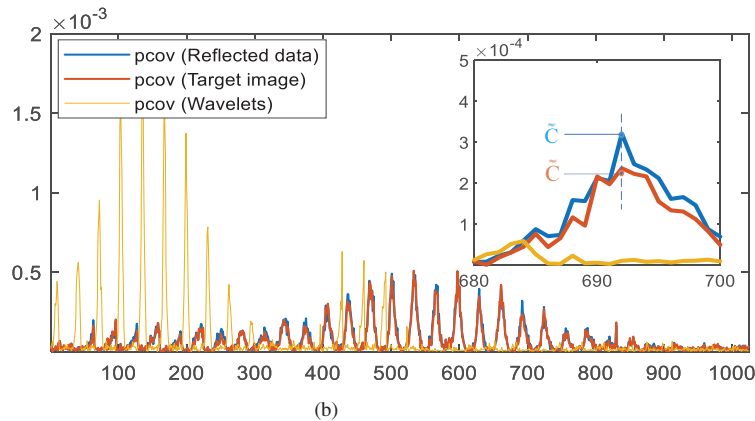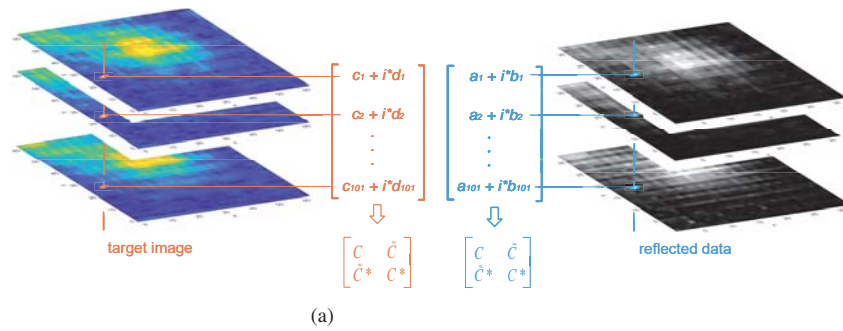
World Academy of Science, Engineering and Technology
International Journal of Electronics and Communication Engineering
Vol:13, No:5, 2019

(a)

(b)

Fig. 5 (a) Sample sets of both reflected data and target image at the same location is built, for the calculation of augment covariance matrix related to that location. (b) $\check{\mathbf{C}}$ in the partial enlarged drawing are computed based on the sample sets given above, and the rest pseudo covariances are calculated in the same manner; and the resultant plots consist of pseudo covariances of the reflected data, the target image, and the wavelets coefficients, each of which has 1024 elements

analytically calculated, such as quantized systems which is not suitable for our case.

Third, we update the mean of component-wise widely linear MMSE estimation based on the impropriety information from the measurement data.

In order to keep notation consistent with that used by [18], we use A to denote the sensing matrix ($A = \Phi$).

A. The Generic GrSBL Algorithm

We begin with a generalized linear models (GLM), shown in Fig. 6 (a), upon which the sparse recovery algorithm is built.
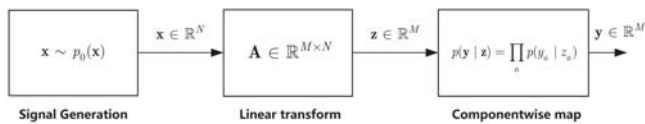

Fig. 6 The generalized linear models (GLM)

The signal $\mathbf{x} \in \mathbb{R}^N$ is assumed to follow a prior distribution $p_0(\mathbf{x})$. $\mathbf{A} \in \mathbb{R}^{M \times N}$ is a known sensing matrix and the sampling rate is $\delta = M/N$. The map of each measurement vector $y \in \mathbb{R}^M$ and $\mathbf{z} = \mathbf{A}\mathbf{x}$ pair can be characterized by fully factorized marginal distribution

$$p(\mathbf{y}|\mathbf{z}) = \prod_{a=1}^{M} p(y_a|z_a) = \prod_{a=1}^{M} p\left(y_a|z_a = \sum_{i=1}^{N} A_{ai}x_i\right). \quad (16)$$

The goal of GLM inference is find the minimum mean square error (MMSE) estimation of underlying signal $\mathbf{x}$, which is the hidden variable in $\mathbf{z} = A\mathbf{x}$. By applying the unified Bayesian inference framework, the GLM inference can be decomposed into two modules: an standard linear model (SLM) inference (module A in Fig. 7 (a)) and a MMSE estimation (module B in Fig. 7 (a)). The original GLM inference can be performed by alternating between the two modules in a turbo manner [3].

GrSBL algorithm begins with placing Gaussian distribution as prior over $\mathbf{z} \sim \mathcal{N}(\mathbf{z}_A^{\text{ext}}, \mathbf{v}_A^{\text{ext}})$, and performing component-wise MMSE estimate in module B, with outputs $\tilde{\mathbf{y}}$ and $\tilde{\boldsymbol{\sigma}}^2$. Then, a sparse Bayesian learning built upon $\tilde{\mathbf{y}} = \mathbf{A}\mathbf{x} + \tilde{\mathbf{w}}$ proceeds in module A, and thereafter mean and variance of $\mathbf{z}$ are updated as $\mathbf{z}_A^{\text{ext}}$ and $\mathbf{v}_A^{\text{ext}}$. This process is repeated till convergence.

B. The Modified GrSBL Algorithm

We extend the original GrSBL algorithm by introducing two sub-modules in module B: the component-wise linear MMSE sub-module and the component-wise widely linear MMSE sub-module [14]. It is assumed that target image is sparse in wavelets domain, which is the necessary condition for a successful recovery. Therefore, we use $\mathbf{x}$ to represent the underlying wavelets coefficients, which has no clear connection between neither the reflected data nor the target image, in terms of pseudo covariance, as illustrated in Fig. 5

World Academy of Science, Engineering and Technology
International Journal of Electronics and Communication Engineering
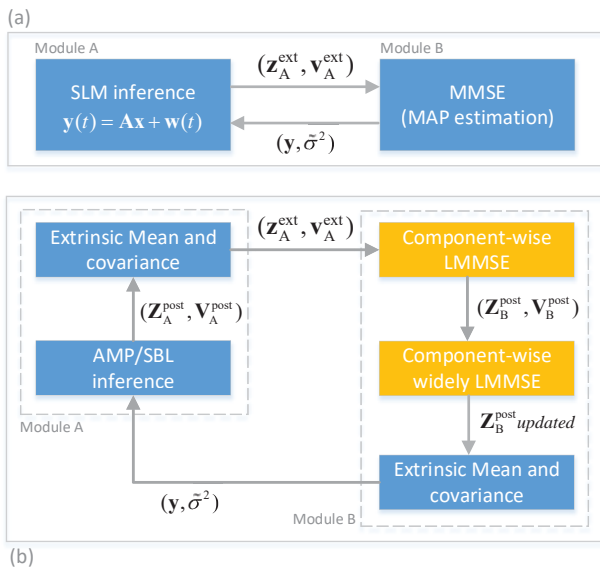Vol:13, No:5, 2019

(a)

(b)

Fig. 7 (a) unified Bayesian inference framework for GLM. (b) The modified framework, where (yellow) rectangle modules 'Component-wise LMMSE' and 'Component-wise widely LMMSE' are introduced

(b).

In order to utilize the pseudo covariance relationship, we perform an additional widely linear estimation upon $\Phi_3^T \mathbf{x}$, which represents the estimated target image. It is worth noting that, according to the uncertainty principle in signal processing, one can not estimate the variance (or uncertainty) in spatial domain and the wavelets domain simultaneously. Thus, the additional widely linear estimation only updates the estimated expectation, and thereafter the estimated target image $\Phi_3^T \mathbf{x}$ is transformed into $\mathbf{z}_b^{\text{post}} = \Phi_1 \circ \Phi_2^T * (\Phi_3^T \mathbf{x})$. Then the inference in module A proceeds, as shown in Fig. 7 (b).

Specifically, at the t-th iteration, $\mathbf{z}_A^{\text{ext}}(t-1)$ and $\mathbf{v}_A^{\text{ext}}(t-1)$ are feed into module sub-module component-wise LMMSE as inputs, and the corresponding outputs reads [3]

$$z_{a,B}^{\text{post}} = A\left(x_{a,A}^{\text{ext}}(t-1) + \mathbf{E}_{\text{CL}}\left(y_a - A x_{a,A}^{\text{ext}}(t-1) \right) \right), \quad (17)$$

with $\mathbf{E}_{\text{CL}} = \mathbf{DC}_{\text{xy}}\mathbf{C}_{yy}^{-1}$, where the elements of the real diagonal matrix $\mathbf{D}$ are

$$[\mathbf{D}]_{i,i} = \frac{v_{a,A}^{\text{ext}}(t-1)}{\mathbf{C}_{x_i y}\mathbf{C}_{yy}^{-1}\mathbf{C}_{yx_i}} \quad (18)$$

where $\mathbf{C}_{xy} = \mathbf{C}_{xx}A^H$ and $\mathbf{C}_{yy} = A\mathbf{C}_{xx}A^H + \mathbf{C}_{nn}$. $\mathbf{C}_{xx}$ in our case is a diagonal matrix, $\mathbf{C}_{xx} = \text{diag}\{v_{a,A}^{\text{ext}}(t-1)\}$; and $\mathbf{C}_{nn}$ contains the variance of the measurement noise, which is also a diagonal matrix. The variance of $\mathbf{z}$ is updated via

$$v_{a,B}^{\text{post}} = \frac{\left(v_{a,A}^{\text{ext}}(t-1)\right)^2}{\mathbf{C}_{z_i y}\mathbf{C}_{yy}^{-1}\mathbf{C}_{yz_i}} - v_{a,A}^{\text{ext}}(t-1) \quad (19)$$

Next, the estimated expectation $\mathbf{z}_B^{\text{post}}$ is updated by performing a component-wise widely LMMSE [14], based on $\mathbf{v}_B^{\text{post}}$ and the impropriety information from measurement

[3] $z_{a,A}^{\text{ext}}(t) = A x_{a,A}^{\text{ext}}(t)$ where $\mathbf{x}$ denote the underlying wavelets coefficients.

data. Specifically, in the update process of $\mathbf{z}_B^{\text{post}}$, in order to utilize the pseudo covariance information, the corresponding constraint should be imposed onto the estimated target image, rather than $\mathbf{z}$. Therefore, component-wise widely LMMSE estimator of the target image $\hat{\mathbf{t}}_{\text{IMG}}$ [4] is to be found as [14]

$$\hat{\mathbf{t}}_{\text{IMG}} = E_{\mathbf{t}}[\mathbf{t}] + \mathbf{W}_{\text{CWL}}\left(\underline{\mathbf{y}} - E_{\mathbf{y}}[\underline{\mathbf{y}}]\right) \quad (20)$$

with $\mathbf{W}_{\text{CWL}} = [\mathbf{w}_{\text{CWL},1}\mathbf{w}_{\text{CWL},2}\cdots\mathbf{w}_{\text{CWL},n}]^H$ and $\underline{\mathbf{y}}$ denotes the widely linear version of $\mathbf{y}$, where the rows of $\mathbf{W}_{\text{CWL}}$ are given by

$$\mathbf{W}_{\text{CWL}} = [0 \quad 1]\underline{\mathbf{C}}_{\mathbf{t}_i\mathbf{t}_i}(\underline{\mathbf{C}}_{\mathbf{t}_i\mathbf{y}}\underline{\mathbf{C}}_{\mathbf{yy}}^{-1}\underline{\mathbf{C}}_{\mathbf{yt}_i})^{-1}\underline{\mathbf{C}}_{\mathbf{t}_i\mathbf{y}}\underline{\mathbf{C}}_{\mathbf{yy}}^{-1}. \quad (21)$$

As shown in Fig. 8, the calculation of terms $\underline{\mathbf{C}}_{\mathbf{t}_i\mathbf{t}_i}$ and $\underline{\mathbf{C}}_{\mathbf{yt}_i}$ are related to the pseudo covariance of the target image, which can be estimated by that of the measurement data. The details of the calculation is well presented in [21].

Thereafter, we have the updated $\mathbf{z}_B^{\text{post}} = A_t\hat{\mathbf{t}}_{\text{IMG}}$.

$$\mathbf{W}_{\text{CWL}} = [0 \quad 1]\underline{\mathbf{C}}_{\mathbf{t}_i\mathbf{t}_i}(\mathbf{C}_{\mathbf{t}_i\mathbf{y}}\underline{\mathbf{C}}_{\mathbf{yy}}^{-1}\underline{\mathbf{C}}_{\mathbf{yt}_i})^{-1}\mathbf{C}_{\mathbf{t}_i\mathbf{y}}\underline{\mathbf{C}}_{\mathbf{yy}}^{-1}$$
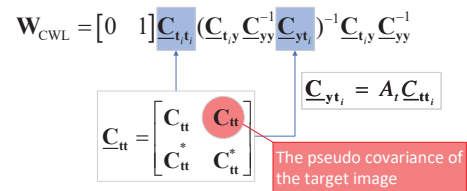

Fig. 8 Relationship of variables or matrices in the process of component-wise widely LMMSE estimation as (21)

Next According to the turbo principle [3], extrinsic mean $\tilde{y}_a(t)$ and variance $\tilde{\sigma}_a^2(t)$ of $\mathbf{z_a}$ are

$$\tilde{\sigma}_a^2(t) = \left(\frac{1}{v_{a,B}^{\text{post}}(t)} - \frac{1}{v_{a,A}^{\text{ext}}(t-1)}\right)^{-1}, \quad (22)$$

$$\tilde{y}_a(t) = \tilde{\sigma}_a^2(t)\left(\frac{z_{a,B}^{\text{post}}(t)}{v_{a,B}^{\text{post}}(t)} - \frac{z_{a,A}^{\text{ext}}(t-1)}{v_{a,A}^{\text{ext}}(t-1)}\right). \quad (23)$$

Messages $\tilde{y}_a(t)$ and $\tilde{\sigma}_a^2(t)$ are delivered to module A to perform the inference, which can be implemented via many variants of SLM inference methods. In this paper, we apply the original approximate message passing (AMP) [9], which belongs to the r-LASSO algorithms [16]. Since our focus is on the modification of module B, the AMP algorithm is simply treated as a black-box function. Detailed implementation of the AMP algorithm can be found in [16], [9].

Similarly, calculations according to turbo principle is performed when messages passing from module A to module B, given as [12]

$$v_{a,A}^{\text{ext}}(t) = \left(\frac{1}{v_{a,A}^{\text{post}}(t)} - \frac{1}{\tilde{\sigma}_a^2(t)}\right)^{-1} \quad (24)$$

$$z_{a,A}^{\text{ext}}(t) = v_{a,A}^{\text{ext}}(t)\left(\frac{z_{a,A}^{\text{post}}(t)}{v_{a,A}^{\text{post}}(t)} - \frac{\tilde{y}_a(t)}{\tilde{\sigma}_a^2(t)}\right). \quad (25)$$

The resultant algorithm is summarized as

[4] We denote $\mathbf{t} = \Phi_2^T * \mathbf{x}_B^{\text{post}}$ and $\mathbf{A_t} = \Phi_1 \circ \Phi_2^T$, for the domain transform.
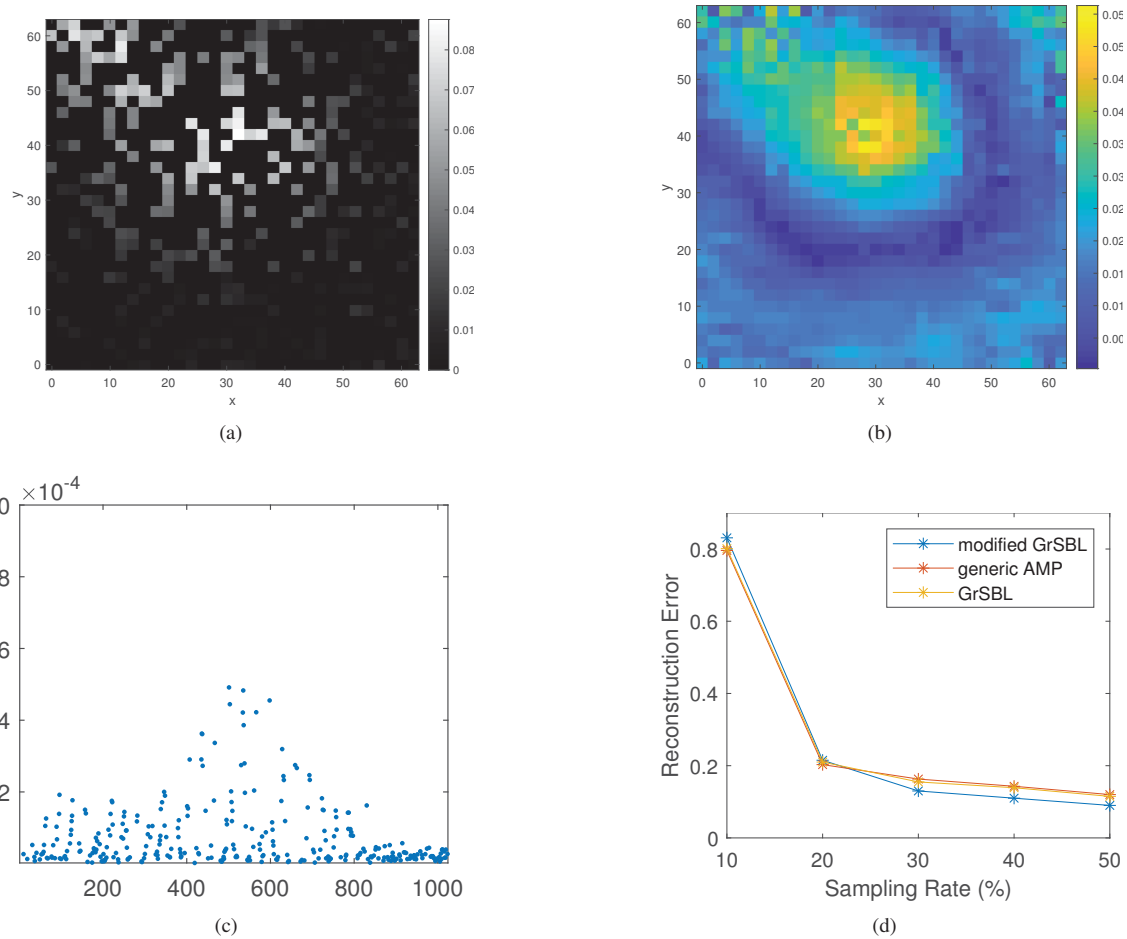
(a)

(b)

(c)

(d)

Fig. 9 (a) The 30 percent sampling in the single-frequency test, operating at 19.26 GHz. (b) reconstruction of the modified GrSBL algorithm at 30 percent sampling rate. (c) The pseudo covariance of the 30 percent sampled data, which is calculated as (15). (d) The construction performance of the different algorithms from 10 to 50 percent sampling rate

---

Algorithm 1 Modified GrSBL algorithm

1: Initialization: $\mathbf{v}_A^{ext}(0)$, $\mathbf{z}_A^{ext}(0)$, $\tilde{\mathbf{C}}_{xx}$;
2: Component-wise LMMSE estimation for $\mathbf{z}_B^{post}$ as (17) and $\mathbf{v}_B^{post}$ as (19);
3: Component-wise widely LMMSE estimation for $\mathbf{z}_B^{post}$ as (20);
4: Extrinsic information: $\tilde{\sigma}^2 = \mathbf{v}_B^{ext}$ and $\tilde{\mathbf{y}} = \mathbf{z}_B^{ext}$, as (22) and (23)
5: AMP inference with Iter_{SLM} iterations over $\tilde{\mathbf{y}} = \mathbf{A}\mathbf{x} + \tilde{\mathbf{w}}$, where $\tilde{\mathbf{w}} \sim \mathcal{N}\left(\tilde{\mathbf{w}}; \mathbf{0}, \text{diag}\left(\tilde{\boldsymbol{\sigma}}^2\right)\right)$;
Outputs: $\mathbf{z}_A^{post}$ and $\mathbf{v}_A^{post}$;
6: Extrinsic information: $\mathbf{v}_A^{ext}$ in (24), and $\mathbf{z}_A^{ext}$ in (25)
7: Repeats until convergence.

V. Numerical Results

In this section, we evaluate the performances of GrSBL [18], modified GrSBL, genenric AMP [16], by performing single-frequency 2-D SAR imaging with compressed measurements. Note that, the original GrSBL algorithm can only deal with quantized compressive sensing problems due to requirement of explicit expression of the posterior. Therefore, we replace the MMSE module with the component-wise LMMSE.

The measurement setting is described in Section III. We perform the test with sampling rate ranged from 10 percent to 50 percent, and for each setting, result is averaged over 100 test runs. The normalized mean square error (NMSE) is defined as $(\|\hat{\mathbf{x}} - \mathbf{x}\|_2 / \|\mathbf{x}\|_2)$.

For Gr-SBL and modified Gr-SBL, the number of inner loop $\text{Iter}_{LSM} = 1$, and message $\mathbf{z}$ is initialized with $\mathbf{z}_A^{ext}(0) = 0, \mathbf{v}_A^{ext}(0) = 10^8$.

Fig. 9 (a) shows the 30 percent random distributed samples for the single-frequency measurement, which is operating at 19.26 GHz; and Fig. 9 (b) shows the corresponding reconstructed target image.

Fig. 9 (c) represents the pseudo covariance of the complex-valued reflected data with respect to the 30 percent samples illustrated in Fig. 9 (a). For missing pseudo covariance, we conduct a 1-D interpolation (FFT method). Results is presented in Fig. 9 (d), the modified GrSBL algorithm achieves better performance with samping rate from 30 to 50 percent over the Gr-SBL and generic AMP.

Compared with GrSBL, the modified algorithm only changes the MMSE method in module B, which considers the second-order non-circularity information. The GrSBL

World Academy of Science, Engineering and Technology
International Journal of Electronics and Communication Engineering
Vol:13, No:5, 2019

performs slightly better than the original AMP.

At lower sampling rate, difference in performance is not significant. The modified GrSBL even output poor results, which may be caused by the inaccurate pseudo covariance estimation, due to insufficient measurement data.

VI. CONCLUSION

In this paper, we extend the generalized sparse Bayesian learning algorithm to deal with the improper complex-valued signal processing problem: the 2-D near-field SAR imaging with under-sampled measurements. Specifically, we perform 2-D image recovery by using single frequency raw data and statistics information from multi-frequencies measurements. In addition, we extend the generalized sparse Bayesian learning by implementing the MMSE module via component-wise widely linear MMSE, to handle general compressive sensing problem, rather than merely quantized system. Numerical results show that the proposed algorithm outperforms the algorithms with conventional proper assumption.

ACKNOWLEDGMENT

REFERENCES

[1] Tülay Adali, Peter J Schreier, and Louis L Scharf. Complex-valued signal processing: The proper way to deal with impropriety. *IEEE Transactions on Signal Processing*, 59(11):5101–5125, 2011.

[2] Maher Al-Shoukairi, Philip Schniter, and Bhaskar D Rao. A gamp-based low complexity sparse bayesian learning algorithm. *IEEE Transactions on Signal Processing*, 66(2):294–308, 2018.

[3] Claude Berrou and Alain Glavieux. Near optimum error correcting coding and decoding: Turbo-codes. *The best of the best: fifty years of communications and networking research*, 45, 2007.

[4] Dongjie Bi, Yongle Xie, Xifeng Li, and Yahong Rosa Zheng. Efficient 2-d synthetic aperture radar image reconstruction from compressed sampling using a parallel operator splitting structure. *Digital Signal Processing*, 50:171–179, 2016.

[5] Dongjie Bi, Yongle Xie, Lan Ma, Xifeng Li, Xiahan Yang, and Yahong Rosa Zheng. Multifrequency compressed sensing for 2-d near-field synthetic aperture radar image reconstruction. *IEEE Transactions on Instrumentation and Measurement*, 66(4):777–791, 2017.

[6] Emmanuel J Candès and Michael B Wakin. An introduction to compressive sampling [a sensing/sampling paradigm that goes against the common knowledge in data acquisition]. *IEEE signal processing magazine*, 25(2):21–30, 2008.

[7] Matteo Carlin, Paolo Rocca, Giacomo Oliveri, Federico Viani, and Andrea Massa. Directions-of-arrival estimation through bayesian compressive sensing strategies. *IEEE Transactions on Antennas and Propagation*, 61(7):3828–3838, 2013.

[8] Müjdat Çetin and William Clement Karl. Feature-enhanced synthetic aperture radar image formation based on nonquadratic regularization. *IEEE Transactions on Image Processing*, 10(4):623–631, 2001.

[9] David L Donoho, Arian Maleki, and Andrea Montanari. Message passing algorithms for compressed sensing: I. motivation and construction. In *2010 IEEE Information Theory Workshop on Information Theory (ITW 2010, Cairo)*, pages 1–5. IEEE, 2010.

[10] Joachim HG Ender. On compressive sensing applied to radar. *Signal Processing*, 90(5):1402–1414, 2010.

[11] Hichem Guerboukha, Kathirvel Nallappan, and Maksim Skorobogatiy. Exploiting k-space/frequency duality toward real-time terahertz imaging. *Optica*, 5(2):109–116, 2018.

[12] Qinghua Guo and Defeng David Huang. A concise representation for the soft-in soft-out lmmse detector. *IEEE Communications Letters*, 15(5):566–568, 2011.

[13] Gabor Hannak, Alessandro Perelli, Norbert Goertz, Gerald Matz, and Mike E Davies. Performance analysis of approximate message passing for distributed compressed sensing. *IEEE Journal of Selected Topics in Signal Processing*, 12(5):857–870, 2018.

[14] Mario Huemer, Oliver Lang, and Christian Hofbauer. Component-wise conditionally unbiased widely linear mmse estimation. *Signal Processing*, 133:227–239, 2017.

[15] Sergey Kharkovsky and Reza Zoughi. Microwave and millimeter wave nondestructive testing and evaluation-overview and recent advances. *IEEE Instrumentation & Measurement Magazine*, 10(2):26–38, 2007.

[16] Arian Maleki, Laura Anitori, Zai Yang, and Richard G Baraniuk. Asymptotic analysis of complex lasso via complex approximate message passing (camp). *IEEE Transactions on Information Theory*, 59(7):4290–4308, 2013.

[17] Xiangming Meng, Sheng Wu, Linling Kuang, and Jianhua Lu. Concise derivation of complex bayesian approximate message passing via expectation propagation. *arXiv preprint arXiv:1509.08658*, 2015.

[18] Xiangming Meng, Sheng Wu, and Jiang Zhu. A unified bayesian inference framework for generalized linear models. *IEEE Signal Processing Letters*, 25(3):398–402, 2018.

[19] Xiangming Meng and Jiang Zhu. A generalized sparse bayesian learning algorithm for 1-bit doa estimation. *IEEE Communications Letters*, 22(7):1414–1417, 2018.

[20] Meenu Rani, SB Dhok, and RB Deshmukh. A systematic review of compressive sensing: Concepts, implementations and applications. *IEEE Access*, 6:4875–4894, 2018.

[21] Peter J Schreier and Louis L Scharf. *Statistical signal processing of complex-valued data: the theory of improper and noncircular signals*. Cambridge university press, 2010.

[22] David M Sheen, Douglas L McMakin, and Thomas E Hall. Three-dimensional millimeter-wave imaging for concealed weapon detection. *IEEE Transactions on microwave theory and techniques*, 49(9):1581–1592, 2001.

[23] Qisong Wu, Yimin D Zhang, Moeness G Amin, and Braham Himed. Complex multitask bayesian compressive sensing. In *2014 IEEE International Conference on Acoustics, Speech and Signal Processing (ICASSP)*, pages 3375–3379. IEEE, 2014.

[24] Zhimin Xu, Wai Lam Chan, Daniel M Mittleman, and Edmund Y Lam. Sparse reconstruction of complex signals in compressed sensing terahertz imaging. In *Signal Recovery and Synthesis*, page STuA4. Optical Society of America, 2009.

[25] Muhammet Emin Yanik and Murat Torlak. Near-field mimo-sar millimeter-wave imaging with sparsely sampled aperture data. *IEEE Access*, 7:31801–31819, 2019.

[26] Siwei Yu, A Shaharyar Khwaja, and Jianwei Ma. Compressed sensing of complex-valued data. *Signal Processing*, 92(2):357–362, 2012.